Check for updates

www.advmattechnol.de

Process Parameter Optimization of Directed Energy Deposited QT17-4+ Steel

Vyas Mani Sharma, Vladimir Popov, Amir R. Farkoosh, Dieter Isheim, David N. Seidman, and Noam Eliaz*

The feasibility of using argon-atomized QT 17-4+ stainless steel powder for directed energy deposition (DED) additive manufacturing is studied. The QT 17-4+ steel is a novel martensitic steel designed based on the compositional modification of the standard 17-4 precipitation-hardened (PH) stainless steel. This modification aims to achieve better mechanical properties of as-deposited components compared to the heat-treated wrought 17-4PH steel. In this study, QT 17-4+ steel powder is used for DED, for the first time. The influence of laser power, laser scan speed, powder feed rate, and hatch overlap on the density is studied. The central composite design is used to determine the experimental matrix of these factors. The response surface methodology is used to obtain the empirical statistical prediction model. Both columnar and equiaxed parent austenite grain structures are observed. X-ray diffraction analyses reveal a decrease in the percentage of retained austenite from 19% in the powder to 5% after DED. The microhardness of the DED processed sample in the as-deposited state is slightly higher than that of wrought 17-4PH steel either solution-annealed or H900-aged. A higher 0.2% yield strength, a lower ultimate tensile strength, and lower elongation are observed for the vertically printed test sample, when compared to the horizontal one.

V. M. Sharma, V. Popov, N. Eliaz
Department of Materials Science and Engineering
Tel-Aviv University
Ramat Aviv. Tel Aviv 6997801 Jerael

Ramat Aviv, Tel Aviv 6997801, Israel E-mail: neliaz@tauex.tau.ac.il

A. R. Farkoosh, D. Isheim, D. N. Seidman Department of Materials Science and Engineering Northwestern University

Evanston, IL 60208, USA

A. R. Farkoosh, D. Isheim, D. N. Seidman Northwestern University Center for Atom-Probe Tomography (NUCAPT) Evanston, IL 60208. USA

The ORCID identification number(s) for the author(s) of this article can be found under https://doi.org/10.1002/admt.202400024

© 2024 The Authors. Advanced Materials Technologies published by Wiley-VCH GmbH. This is an open access article under the terms of the Creative Commons Attribution-NonCommercial-NoDerivs License, which permits use and distribution in any medium, provided the original work is properly cited, the use is non-commercial and no modifications or adaptations are made.

DOI: 10.1002/admt.202400024

1. Introduction

Directed energy deposition (DED) and selective laser melting (SLM) are the most commonly used powder-based additive manufacturing (AM) techniques to fabricate dense metallic parts.[1,2] In these processes, a molten pool is formed by the interaction of laser and feedstock powder.[3] Intense localized heat input and a short interaction time result in high cooling rates and high-temperature gradients in both DED and SLM.[4] DED is regarded as one of the most efficient AM processes for producing and repairing high-volume components. Because of the direct injection of metal powder into the heat source in the DED system, it is possible to print parts onto curved surfaces. The precise deposition capacity of DED offers various advantages. It allows accurate deposition of fine lines or small areas, enabling applications such as repairing damaged components, protecting particular sites from corrosion, and providing wear-resistant coating.^[5,6] High-performance materials, such as functionally graded materials,

composites, ceramics, shape memory alloys, intermetallic, highentropy alloys, aluminum alloys, nickel-based alloys, cobalt-based alloys, titanium-based alloys, alloy steels, tool steels, and stainless steels can be processed using DED.^[7,8] Controlling the variation in the microstructure and mechanical properties of the DED'ed parts is still challenging. The control of process parameters significantly affects the material density and microstructure evolution. Optimization of process parameters is essential to ensure the desired material properties, structural integrity, and functional characteristics of the AM'ed parts.^[9–11]

17-4 precipitate-hardened (PH) steel is widely used in chemical, nuclear, power plants, aircraft, and marine industries because of its high corrosion resistance, strength, and mechanical properties below 300 °C.^[12-17] A combination of sub-micron size copper precipitates and martensitic microstructures is the main reason for the high strength.^[18,19] Solution-annealed 17-4PH steel comprises lath martensite, whereas the AM'ed 17-4PH steel exhibits a varied microstructure.^[20,21] In earlier studies of AM, the high cooling rate resulted in microstructural variations along the build direction and perpendicular to the build direction.^[22-25]



Anisotropy and pores formed during AM restrict reliability and service life. [26] Hence, process parameters must be optimized to reduce porosity and anisotropy and enhance product quality. Yu et al. sought to minimize the need for post-heat treatments when using DED combined with ultrasonic vibration (UV) to fabricate 17-4 PH. [19] Such an approach resulted in a large number density of nanoscale Cu-rich precipitates responsible for strengthening the as-printed steel.

The volume fraction of retained austenite in the as-printed 17-4PH steel significantly depends on the processing parameters and the powder atomization environment (Ar or $\rm N_2$ gas). $^{[13,14,27]}$ Murr et al. $^{[14,27]}$ reported the martensitic structure of 17-4PH steel fabricated using SLM in $\rm N_2/Ar$ (AM environment/powder atomization), $\rm Ar/N_2$, and $\rm Ar/Ar$ atmospheres; the percentage of martensite reduced in the $\rm N_2/N_2$ atmosphere.

Khalid et al.^[13] reported a predominantly austenitic (FCC) microstructure in AM'ed parts fabricated in the N₂ atmosphere, regardless of the powder atomization environment. Nezhadfar et al.^[28] performed a comparative experimental study of SLM'ed and DED'ed 17-4 PH specimens. They observed the presence of coarse massive ferrite in parts fabricated by DED, whereas parts processed by SLM exhibited equiaxed ferrite and lath martensite. Pan et al. reported the successful application of wire-arc DED for 17-4 PH steel.^[29] A two-step post-processing heat treatment was, however, necessary to enhance the microhardness and corrosion resistance.

Li et al.[30] performed a process parameter optimization for depositing SS 316L powder on Inconel substrate and analyzed the effect of laser spot size, laser power, powder mass flow rate (PMFR), laser scan speed, and shielding gas flow on the deposition. The best combination of process parameters for good adhesion of metal powder to an Inconel substrate was obtained when the metal powder and substrate commenced melting. The metal powder was spread over the substrate at a low PMFR, whereas the particles rebounded at a higher PMFR. Zhang et al.[31] observed an improved tensile strength, yield strength, and microhardness with increasing laser scan speed for AM'ed SS 316. Amar et al.[32] investigated the effect of PMFR, laser scan speed, and laser power on microhardness, density, and layer thickness of DED'ed 316L steel using the response surface methodology (RSM). They observed that the PMFR has a detrimental effect on the density and microhardness; the single-layer height increased with an increase in laser power and PMFR. Morales et al.[33] performed single-track DED trials using 17-4 PH powder. They observed a reduced volume fraction of the δ -ferrite (BCC structure) and a higher microhardness of the samples produced at lower laser power and laser scan speed.

In this study, we utilize DED to fabricate a new steel powder, QT 17-4+, developed recently for AM by QuesTek Innovations LLC (Evanston, IL). Critical process parameters, such as laser power, laser scan speed, powder feed rate (PFR), and hatch overlap were optimized to achieve the highest possible density. The hatch overlap (expressed as a percentage of the hatch spacing) dictates the amount of area where multiple scan paths intersect and molten material accumulates. Central composite design (CCD) and RSM were used to develop a quadratic prediction model equation for density. Furthermore, the influence of linear, quadratic, and interaction factors on the predicted density

Table 1. Factors and their levels used for the central composite design.

| Factors | Units | | Factor Level | | | | | |
|----------------------|----------------------|--------|--------------|-------|-------|-------|--|--|
| | | a (-2) | -(1) | 0 | +(1) | A(2) | | |
| Laser power [P] | W | 275 | 350 | 425 | 500 | 575 | | |
| Scan speed [V] | ${\rm mm\ min^{-1}}$ | 534 | 610 | 686 | 762 | 838 | | |
| Powder feed rate [m] | rpm | 3.25 | 4 | 4.75 | 5.5 | 6.25 | | |
| Hatch overlap | % | 37.5 | 50.00 | 62.50 | 75.00 | 87.50 | | |

was analyzed. Samples were then fabricated for mechanical and microstructural characterization using the optimum process parameters.

2. Results and Discussion

2.1. Design of Experiments for DED Processing of a QT17-4+ Steel

QT 17-4+ steel powder was successfully used to manufacture by DED cubic coupons as per the rotatable CCD matrix. Table 1 provides the factors and the levels used for CCD. **Table 2** shows the four-factor rotatable CCD matrix with response data. The following statistical measures were employed to evaluate the model's suitability: p-value, F-value, assessment of lackof-fit, adjusted R^2 -value, and predicted R^2 -value (R represents the correlation coefficient). The significance of the terms was determined using the p-value, a p-value less than 0.05 indicating a significant term.^[34] A model is considered an excellent fit for an R²value greater than 0.8. Adjusted R^2 -values are reduced when a variable does not significantly affect the model's fit.[35] The predicted R^2 -value represents the model's ability to predict the response to new observations; the higher the predicted R^2 -value, the better the response prediction. An improved model is obtained when the predicted and adjusted R^2 -values are close to one another.[36]

2.2. Response Surface Methodological Approach to Optimize the Process Parameters

This study employs the least-squares method to obtain a second-order quadratic regression model for the density of DED'ed QT 17-4+. Equation (1) presents the developed model with both the linear and quadratic terms. Analysis of variance (ANOVA) was performed to assess the importance and significance of the quadratic density model. To avoid overfitting and enhance model accuracy, non-significant terms were removed. Equation (1) is only valid for the range of variables presented in this work. Table S1 (Supporting Information) shows the ANOVA table of the density model. Here, the *p*-value is less than 0.0001 and the *F*-value is 9.2, which indicates the significance of the model. The regression coefficient *R*²-value is 0.90, and the adjusted *R*²-value is 0.80. The validity and relevance of the model are confirmed with a closer *R*²-value and adjusted *R*²-value.^[37] In the ANOVA table, the residual is defined as the summation of lack-of-fit and

www.advmattechnol.de

Table 2. Experimental matrix with factors and their responses.

| Run I | Pattern | Factors | | | | Response | |
|-------|---------|---------|---------------------------|---------|--------|---------------------------------------|--|
| | | P (W) | V [mm min ⁻¹] | m [rpm] | Н [%] | Density, ρ [g cm ⁻³] | |
| 1 | a000 | 275 | 686 | 4.75 | 62.500 | 7.4973 | |
| 2 | | 350 | 610 | 4 | 50.000 | 7.522 | |
| 3 | + | 350 | 610 | 4 | 75.000 | 7.6101 | |
| 4 | -+- | 350 | 610 | 5.5 | 50.000 | 7.5482 | |
| 5 | -++ | 350 | 610 | 5.5 | 75.000 | 7.5512 | |
| 6 | -+- | 350 | 762 | 4 | 50.000 | 7.5107 | |
| 7 | -+-+ | 350 | 762 | 4 | 75.000 | 7.5027 | |
| 8 | -++- | 350 | 762 | 5.5 | 50.000 | 7.5465 | |
| 9 | -+++ | 350 | 762 | 5.5 | 75.000 | 7.5369 | |
| 10 | 0a00 | 425 | 534 | 4.75 | 62.500 | 7.5773 | |
| 11 | 00a0 | 425 | 686 | 3.25 | 62.500 | 7.5625 | |
| 12 | 000a | 425 | 686 | 4.75 | 37.500 | 7.6289 | |
| 13 | 0000 | 425 | 686 | 4.75 | 62.500 | 7.5423 | |
| 14 | 0000 | 425 | 686 | 4.75 | 62.500 | 7.5539 | |
| 15 | 0000 | 425 | 686 | 4.75 | 62.500 | 7.5555 | |
| 16 | 0000 | 425 | 686 | 4.75 | 62.500 | 7.5493 | |
| 17 | 0000 | 425 | 686 | 4.75 | 62.500 | 7.5577 | |
| 18 | 0000 | 425 | 686 | 4.75 | 62.500 | 7.5671 | |
| 19 | 000A | 425 | 686 | 4.75 | 87.500 | 7.5739 | |
| 20 | 00A0 | 425 | 686 | 6.25 | 62.500 | 7.6068 | |
| 21 | 0A00 | 425 | 838 | 4.75 | 62.500 | 7.5082 | |
| 22 | + | 500 | 610 | 4 | 50.000 | 7.5554 | |
| 23 | +-+ | 500 | 610 | 4 | 75.000 | 7.5924 | |
| 24 | +-+- | 500 | 610 | 5.5 | 50.000 | 7.5734 | |
| 25 | +-++ | 500 | 610 | 5.5 | 75.000 | 7.5926 | |
| 26 | ++- | 500 | 762 | 4 | 50.000 | 7.5748 | |
| 27 | ++-+ | 500 | 762 | 4 | 75.000 | 7.5426 | |
| 28 | +++- | 500 | 762 | 5.5 | 50.000 | 7.6345 | |
| 29 | ++++ | 500 | 762 | 5.5 | 75.000 | 7.5785 | |
| 30 | A000 | 575 | 686 | 4.75 | 62.500 | 7.5792 | |

pure error. Pure error refers to the variability in data that cannot be attributed to the effects of independent variables in a model. A lower F-value indicates the insignificance of lack-of-fit compared to the pure error that confirms the model's accuracy and validity. In the present model, an F-value of 4.67 and a p-value of 0.05 prove the insignificance of lack-of-fit. Hence, the current model is acceptable for predicting the density, ρ , of the printed parts:

$$\rho = 7.689004 + 0.009623H - 0.000078P - 0.216128m$$

$$+0.000179V + 0.000068H^{2} + 0.011717m^{2} - 0.000017H$$

$$\times V + 0.000002 P \times V + 0.000197 m \times V$$
(1)

where H is the hatch overlap, P is laser power, m is PFR, and V is laser scan speed. Table 2 demonstrates that the variation in the laser power, laser scan speed, PFR, and hatch overlap considerably affect the density, but only within the variable factor level. Table S1 (Supporting Information) shows the significance of the linear and quadratic parameters. The significance of the follow-

ing terms was established based on a threshold p-value of less than 0.05: the linear terms for laser power P, V, and m; the interaction terms for laser power and laser scan speed ($P \times V$), scan speed and PFR ($V \times m$), scan speed and hatch overlap ($V \times H$); the quadratic terms of PFR ($V \times m$) and hatch overlap ($V \times m$). We note that the hatch overlap has an insignificant influence on the model, but the interaction and quadratic terms have a significant influence. Hence, the hatch overlap term is not removed from the model, Equation (1).

2.3. The Effect of Individual Parameters

Figure 1a displays the influence of laser power on the steel density at a laser scan rate of 686 mm min⁻¹, a PFR of 4.75 rpm, and a hatch overlap of 62.5%. Figure 1a demonstrates that density increases from 7.53 to 7.57 g cm⁻³ with an increase in laser power from 350 to 500 W. Reduced laser power results in reduced heating, further resulting in weaker bonding between the powder particles. Hence, the porosity increases with reduced laser power. Reheating of the previous layers results in better bonding between the powder particles. Figure 1b displays the influence of laser scan speed at a laser power of 425 W, PFR of 4.75 rpm, and a hatch overlap of 62.5%. The steel density decreases with increasing laser scan speed. The reduced sintering time at higher scan speeds may increase porosity due to inadequate melting and fusion of the powder particles. The density slope is nonlinear, and the density's sensitivity to laser scan speed is smaller at lower scan speeds. The scan speed impacts the molten pool's wetting, morphology, and dimensions, influencing porosity and multi-layer formation. [38] The molten pool's penetration is higher at lower scan speeds, resulting in a consistent molten pool with small porosity. This is due to the fact that laser energy per unit length increases with reduced scan speed.[39] The density variation is minimal when the scan speed increases from 538 to 625 mm min⁻¹, compared to the increase in scan speed from 700 to 787 mm min $^{-1}$.

Figure 1c displays the effect of PFR on the density at a laser power of 425 W, laser scan speed of 686 mm min⁻¹, and a hatch overlap of 62.5%. The density increases with increasing PFR. This may be because when the PFR is small, the volume of particles the gas carries is small. This results in insufficient powder packing and increased gas entrapment. With an increase in PFR, maintaining the rate of the carrier gas constant, the powder particles are closely packed, reducing the gas trapping sites.^[40] This trend is only valid for a specified variable range of PFR at a laser power of 425 W, laser scan speed of 686 mm min⁻¹, and a hatch overlap of 62.5%. This trend is inconsistent with previous studies, which reported an increase in porosity with increasing PFR.[41,42] However, the material and process parameters differ from the currently selected parameters and metal powder. It cannot be extrapolated beyond the factor level range provided in Table 1.

Figure 1d displays the influence of hatch overlap on the density at a laser power of 425 W, laser scan speed of 686 mm min⁻¹, and PFR of 4.75 rpm. Hatch overlapping is a critical parameter influencing the AM'ed parts' defect formation, surface finish, and geometrical characteristics.^[43–45] Higher hatch overlap leads to the remelting of large areas of the deposited

estern University, Wiley Online Library on [28/08/2024]. See the Terms and Conditions (https://onlinelibrary.wiley.com/tern

and-conditions) on Wiley Online Library for rules of use; OA articles are governed by the applicable Creative Commons

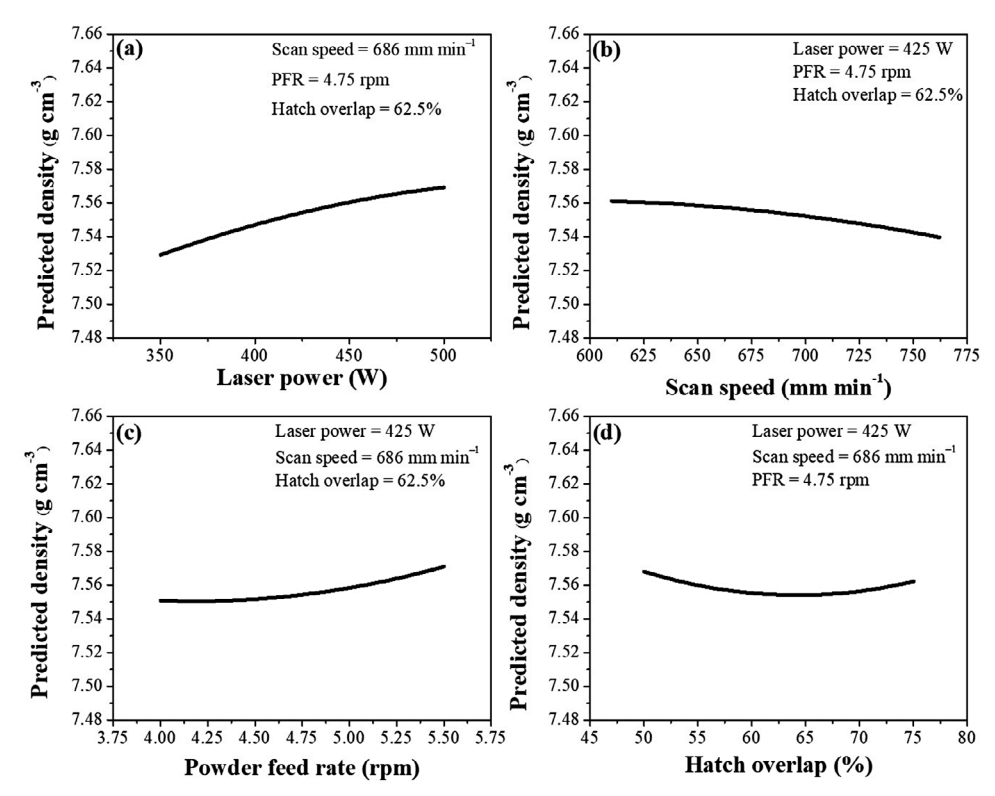


Figure 1. The effects of a) laser power, b) laser scan speed, c) powder feed rate, and d) hatch overlap on the predicted densities of QT17-4+ steel. The density of solution-annealed wrought 17-4PH steel is 7.8 g cm⁻³.

layer, removing the trapped pores. The melting of deposited material increases with increasing hatch overlap, resulting in higher density. Excessive hatch overlap may increase deposition time, porosity, and cracking. High heat generation in the localized areas at higher hatch overlap can cause thermal stresses, forming hot cracks. Hence, for the current research and the variable range level, it is observed that at 50% overlap, the density attains a maximal value. From 50% to 62.5% hatch overlap, the density reduces, and above 62.5% it gradually increases. The increase in the density beyond 62.5% hatch overlap is small.

2.4. Combined Effects of Parameters

One-variable-at-a-time methods are a common approach to experimental design, but they have a significant drawback: they ignore interactions between variables. An interaction occurs when the effect of one variable on the response depends on the value of another variable. One-variable-at-a-time method can fail to detect interactions, leading to inaccurate conclusions about the relationships among variables. Table S1 (Supporting Information) displays the interactions among laser power and laser scan speed, PFR and laser scan speed, and hatch overlap, which are significant in the model, Equation (1). This means removing other interactive terms without sacrificing the model's accuracy is a reasonable approximation.

Figure 2a illustrates the interaction of the laser power at two different laser scan speeds (610 and 762 mm min⁻¹), while the

PFR and hatch overlap were constant at 4.25 rpm and 62.5%, respectively. The convergence of the two plots in Figure 2a at 500 W confirms the interaction between laser power and laser scan speed, as it demonstrates that an identical density value can be obtained with two different sets of processing parameters. It is noted that the predicted density increases with increasing laser power, independent of the laser scan speed. This increase in predicted density is greater for a scan speed of 762 mm min⁻¹ than the 610 mm min⁻¹ for laser power in the 350 to 500 W range. Figure 2b demonstrates how laser power and scan speed interact to affect the predicted density of a part when the PFR and hatch overlap are constant. Combining high laser power and high laser scan speed results in a smaller melt pool width and a larger melt pool volume, an excellent condition for higher density.^[47] Higher laser power and lower laser scan speed produce higher energy density, leading to rapid vaporization, excessive melting, and keyhole porosity formation.[48]

The effect of PFR on the predicted density at two different scan speeds is displayed in Figure 2c, with laser power and hatch overlap maintained constant at 425 W and 62.5%, respectively. The combined effect of laser scan speed and PFR is displayed in Figure 2d. At smaller PFR, the predicted density is larger at 610 mm min⁻¹ than at 762 mm min⁻¹. The difference is negligible at a PFR of 5.5 rpm. The predicted density decreases with increasing PFR at lower scan speed, while the opposite is obtained at high scan speed. Laser scan speed and PFR are two critical parameters that affect the density of the deposited material in DED processes. Lower scan speeds result

2365709x, 2024, 15, Downloaded from https://onlinelibrary.wiley.com/doi/10.1002/admt.202400024 by Northwestern University, Wiley Online Library on [28082024]. See the Terms and Conditi

onditions) on Wiley Online Library for rules of use; OA articles are governed by the applicable Creative Commons

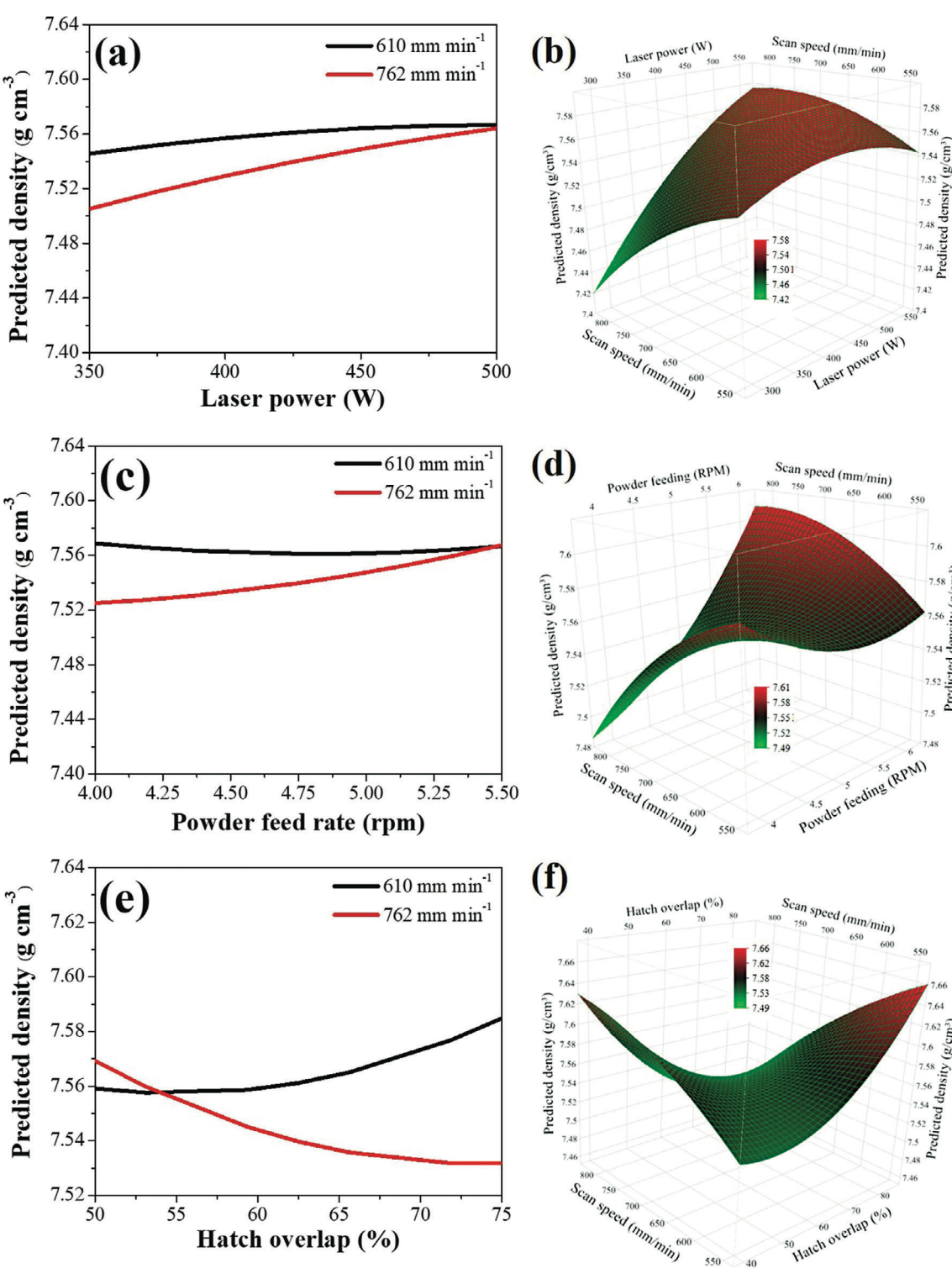


Figure 2. a) Interaction of laser power and scan speed. b) Surface plot showing the combined effect of laser power and scan speed on the predicted density (powder feed rate = 4.75 rpm, hatch overlap = 62.5%). c) Interaction of powder feed rate and laser scan speed. d) Surface plot showing the combined effect of powder feed rate and laser scan speed on the predicted density (laser powder = 425 W, hatch overlap = 62.5%). e) Interaction of hatch overlap and laser scan speed. f) Surface plot showing the combined effect of hatch overlap and laser scan speed on the predicted density (powder feed rate = 4.75 rpm, laser power = 425 W).

and-conditions) on Wiley Online Library for rules of use; OA articles are governed by the applicable Creative Commons

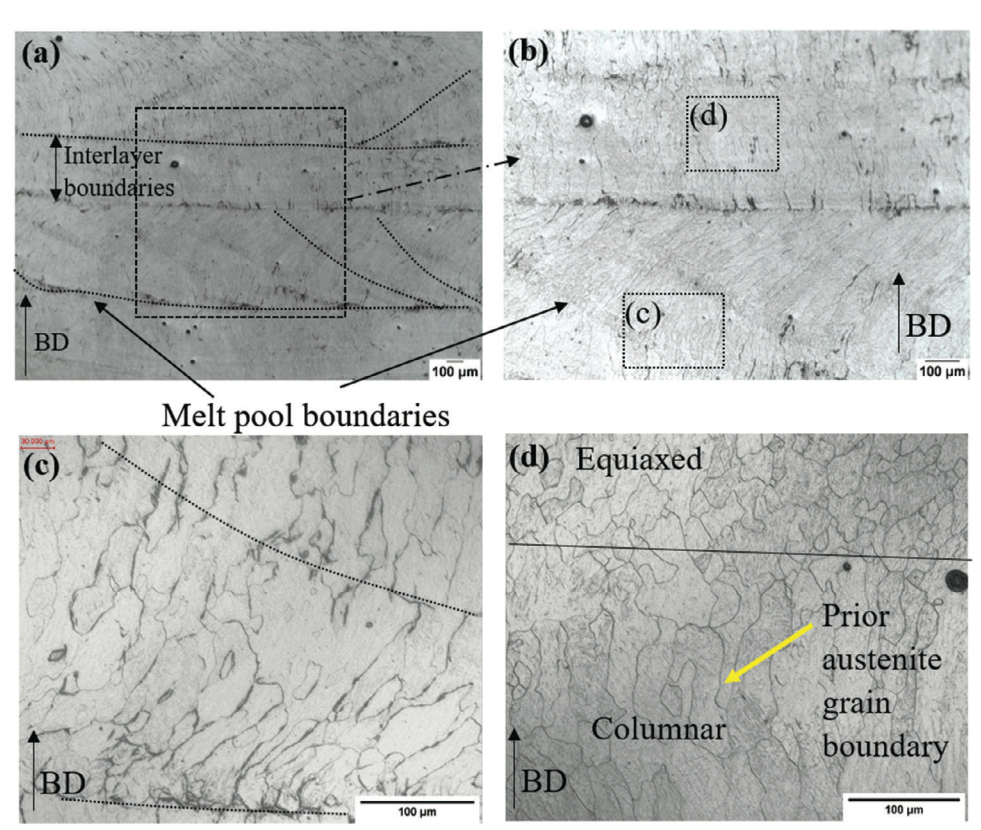


Figure 3. a) Cross-section view of the as-printed DED QT 17-4+ steel after polishing and chemical etching in Kalling's Reagent No. 2 at room temperature. Melt pool boundaries and the interlayer boundary between two layers are revealed. b) An enlarged view of the bottom layer boundary and interlayer boundary in (a). (c) and (d) display the grain diameter and morphology of the layer boundary and interlayer boundary, respectively. BD refers to build direction.

in faster energy input per unit area, allowing for more thorough melting and fusion due to longer dwell times. [49–51] Increasing the PFR too much at lower scan speeds can lead to problems, such as insufficient energy for complete fusion (lack-offusion, LoF) and an increased risk of spattering or melt pool instability.

Alternatively, higher scan speeds reduce the energy input per unit length due to shorter dwell times. Increasing the PFR at higher scan speeds compensates for reduced dwell times, facilitating better fusion and, consequently, higher densities.^[52] This is only correct for the studied range of variable levels, Table 1.

Figure 2e displays the interaction of hatch overlap at two different laser scan speeds, at constant laser power (425 W) and PFR (4.25 rpm). The combined effects of hatch overlap and laser scan speed on the predicted density are demonstrated in Figure 2f. It is noted that at a smaller hatch overlap, the predicted density is smaller for a lower laser scan speed. With an increase in hatch overlap, the density increases rapidly for the lower scan speed, while it decreases sharply for the higher laser scan speed. The interaction between hatch overlap and laser scan speed significantly affects the predicted density of DED'ed deposits. At lower laser scan speeds, the melt pool has more time to solidify. If the hatch overlap is too small, the melt pools from adjacent scan tracks may not overlap sufficiently, resulting in voids, defects, and lower density. Increasing the hatch overlap at lower

laser scan speeds helps reduce voids and gas porosity because the melt pools from adjacent scan tracks overlap more, leading to higher densities. At faster scan speeds, the melt pool has less time to solidify. If the hatch overlap is too high, the melt pools from adjacent scan tracks may overlap too much, leading to instability, defects, and lower densities.^[53–57] Based on the above analyses, the optimal process parameters for laser power, laser scan speed, PFR, and hatch overlap are determined to be 500 W, 762 mm min⁻¹, 5.5 rpm, and 50%, respectively. Thus, we performed a further study of the microstructure and mechanical properties of QT17-4+ steel processed by DED using these optimal processing parameters.

2.5. Microstructural Analyses

Figure 3 displays the microstructure of a DED QT17-4+ sample in the as-printed state. The melt pool boundaries (delineated with dotted lines) and interlayer boundaries are visible in Figure 3a,b. Figure 3c illustrates that the columnar grains are present within the layer boundary and tend to align perpendicular to the melt pool boundary and along the temperature gradient. Different columnar grains traverse multiple melt pools, which strongly suggests epitaxial growth of prior austenite or δ-ferrite grains from one melt pool into another during layer-by-layer fabrication. Figure 3d shows the grain structure distribution

estern University, Wiley Online Library on [28/08/2024]. See the Terms

and-conditions) on Wiley Online Library for rules of use; OA articles are governed by the applicable Creative Commons

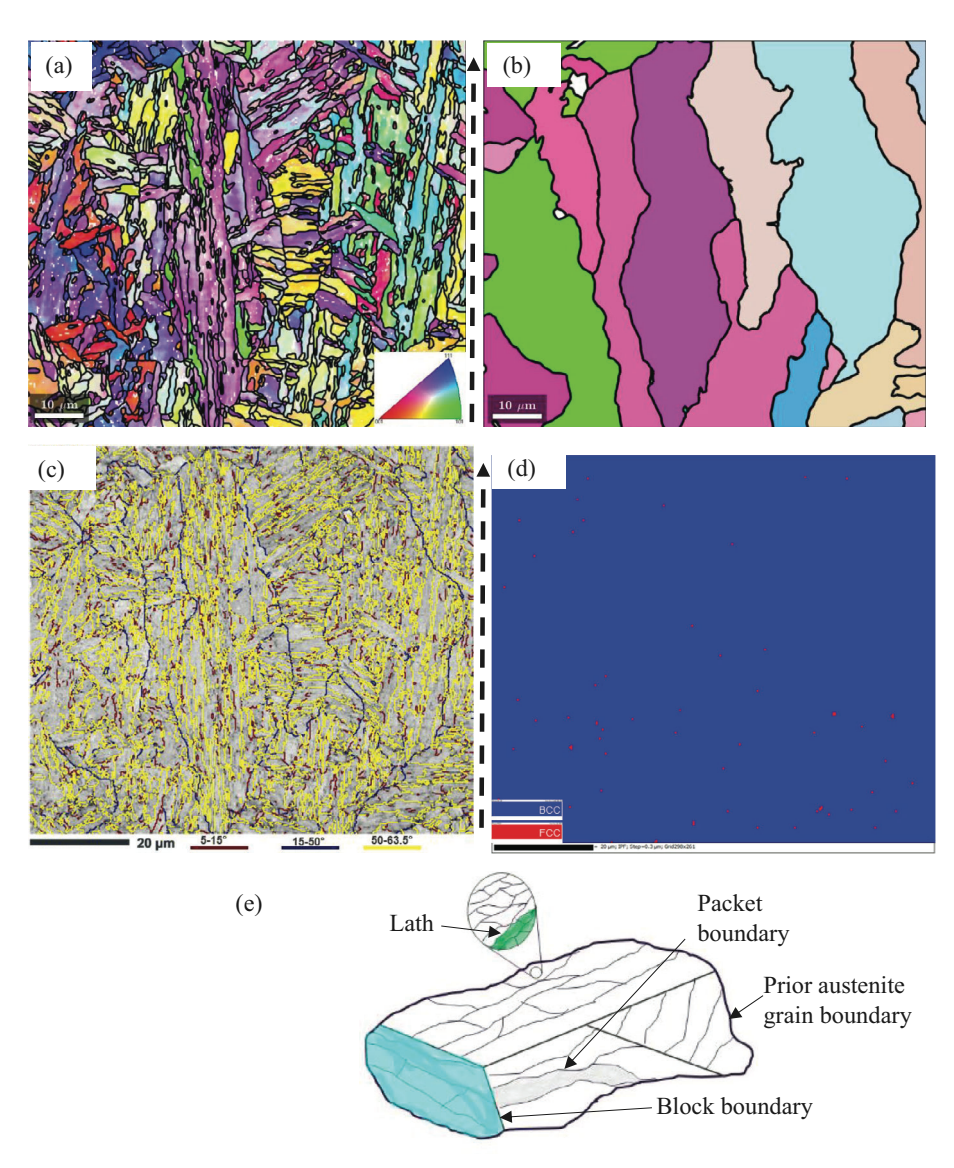


Figure 4. a) An EBSD inverse pole figure map of an as-printed DED QT17-4+ sample in the plane parallel to the build direction. b) Reconstructed prior austenite grains. c) Disorientation boundaries map. d) Phase distribution map. e) Schematic diagram displaying the lath martensite hierarchy. The dashed arrow represents the build direction from bottom to top.

in the interlayer boundary. The solid line distinguishes the columnar grains from the equiaxed grains. Grains are columnar at the start of the interlayer boundary and are perpendicular to the melt-pool layer (along the build direction). The average length of the columnar grains is $136\pm20~\mu\mathrm{m}$. Besides the large columnar grains formed just above the layer boundary, a small equiaxed grain diameter of $36\pm8~\mu\mathrm{m}$ is formed below the next layer. It is noted that the solidification rate (V_{s}) and the temperature gradient (G) mainly influence the grain morphology in AM. In the melt pool, V_{s} decreases and G increases with the depth. [58] Kartavykh et al. [59] observed that columnar grains are formed at small V_{s} and large G values. Due to rapid cooling, equiaxed grains are formed in the top layer of the heat-affected zone (HAZ) during AM. [60,61]

Electron backscatter diffraction (EBSD) analyses were performed to investigate the grain structure, orientation dis-

tribution, and phase constitution in DED QT 17-4+ in a plane parallel to the build direction. **Figure 4a** shows the EBSD map of the printed QT 17-4+ sample. Localized and rapid solidification promote the formation of a combined near-equiaxed and columnar grain structure, also known as a columnar-to-equiaxed transition (CET);^[62] austenite grains transform into martensite upon cooling to room temperature.

The average size of the martensite block is 8.9 ± 6 µm. Figure 4b shows the prior austenite grain boundary. Martensite adopts the Kurdjumov-Sachs (K-S) orientation relationship with respect to the prior austenite grain (PAG). This means that the relative orientation of adjacent martensite laths can be used to reconstruct the prior austenite microstructure. The same approach was used in this article to reconstruct the prior austenite microstructure. PAG are columnar grains oriented along



www.advmattechnol.de

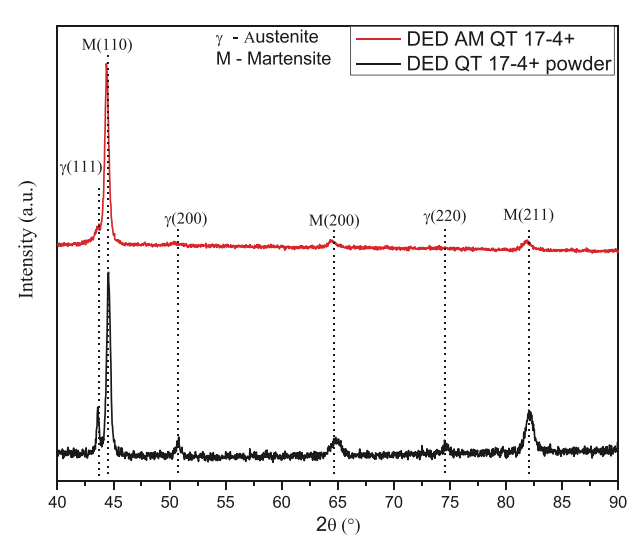


Figure 5. XRD patterns from the QT17-4+ powder and DED'ed QT17-4+ samples in the as-printed state, displaying reflections of the γ -austenite (FCC) and M-martensite (BCT) phases.

the build direction, Figure 4b. Figure 4e presents a schematic diagram of the lath martensite hierarchy, which aids in understanding the martensite phase's misorientation and prior austenite grain boundaries. Figure 4c displays the prior austenite and martensite lath boundary misorientation angles. The misorientation angle between the martensite block is ≈50-60°, whereas the packet boundary has a misorientation angle of 10-20° and 45-60°. Packet boundaries are interfaces between groups of laths in martensitic structures. PAG boundaries have a misorientation angle of 20-60°. Similar observations were made by Karthikeyan et al.[64] for a low-carbon alloy steel. Grain boundaries (GBs) with misorientations between 5° and 15° are classified as low-angle GBs (LAGBs), while GBs with misorientations >15° are classified as high-angle (HAGBs). The percentage of LAGBs and HAGBs is 16.5% and 83.8%, respectively. It is noted that the percentage of HAGBs associated with the PAG boundary is ≈7%, and the remainder is related to lath martensite boundaries. A high dislocation density increases the strength and microhardness of a material, but it can also reduce its ductility. A martensitic transformation during cooling is the main reason for the higher dislocation density of martensite when compared to austenite. Figure 4d shows the phase distribution map: 99.9% martensite (blue background) and 0.09% austenite (red spots). X-ray diffraction (XRD) analyses were performed to obtain the volume fraction of austenite and martensite in the DED'ed steel. Figure 5 displays the XRD patterns from the as-received QT17-4+ powder and QT17-4+ DED'ed at the optimal process parameters. The volume fraction of austenite in the as-synthesized powder is 19 \pm 3%, which reduces to 5 \pm 1% after DED. The difference in the volume fraction of austenite obtained by EBSD and XRD is due to the limited spatial resolution of the EBSD technique, which cannot resolve austenite grains smaller than pprox20–50 nm,^[65] and the small dimensions of the scanned area $(90 \times 80 \, \mu m^2)$.

2.6. Mechanical Properties

Figure 6a compares the Vickers microhardness values for asprinted DED OT17-4+ steel, H900 (peak-aged at 482 °C for 1 h) heat-treated wrought 17-4PH steel, and solution-annealed (annealed at 1038 °C for 30 min, followed by air cooling) wrought 17-4PH steel. DED'ed QT17-4+ steel has a microhardness of \approx 440 \pm 15 VHN in the as-printed state, slightly higher than that of heat-treated wrought 17-4PH (430 \pm 11 VHN). The enhanced microhardness is due to a finer grain size, a higher dislocation density, and a much higher carbon concentration in DED QT17-4+ (0.17 vs 0.03 wt.% in the wrought steel). Choo et al. [66] measured the microhardness of DED'ed 17-4PH and heat-treated DED 17-4PH steel as 354 and 361 VHN, respectively. The increase in the microhardness after heat treatment was due to the formation of copper-rich precipitates. The microhardness of the QT17-4+ steel is thus 25% higher than that of a "standard" DED 17-4PH steel in the as-printed state. [66]

Figure 6b displays a stress-strain plot of QT17-4+ steel DED'ed under the optimal process parameters. Force and strain values were obtained from the load cell and DIC analysis, respectively. Tensile tests were performed for both horizontally and vertically built specimens, Figure S3 (Supporting Information). The higher 0.2% offset yield strength observed for the verticallybuilt specimens (757 \pm 14 MPa), when compared to horizontallybuilt specimens (552 \pm 12 MPa) indicates an anisotropy of the mechanical properties, which is attributed to the presence of elongated grains aligned along the build direction, resulting in the development of crystallographic texture. The ultimate tensile strength (UTS) of the vertically built specimens is 1592 ± 6 MPa, while for the horizontally built specimens, it is 1625 ± 39 MPa. Young's modulus values of 200 \pm 19 GPa and 251 \pm 2 GPa are obtained for the horizontal and vertical samples, respectively. Eskandari et al. reported 209 ± 14 GPa as Young's modulus of wrought 17-4PH steel.^[67] The variation in Young's modulus values can be related to crystallographic anisotropy of the DED'ed specimens as well as to different microstructures and porosity levels.

Figure 7 displays fractographic images of tensile test specimens after fracture. The fracture surface of a horizontally printed specimen exhibits a brittle quasi-cleavage failure mode, Figure 7a. At a lower magnification, a relatively flat surface with pores is observed. A river pattern is also observed, indicating brittle fracture. The crack propagates from the interface of the sample to the middle of the AM'ed portion. In the horizontal sample, the fracture occurs without necking. At higher magnifications, fine dimples are observed, indicating ductile fracture. It is concluded that the fracture of the horizontal sample has a mixed failure mode. The ductile fracture occurs later in the failure process after the crack has significantly propagated. Figure 7b displays the fractography of a vertically printed tensile sample. The tensile test direction is perpendicular to the layer boundary for the vertical samples. Delamination, leading to the formation of a crack along the cross-sectional area, is evident in Figure 7d. Intergranular fracture is seen at high-magnification scanning electron microscope (SEM) images of the fracture surface. Crack propagation is through the melt pool and melt-pool boundaries. Micro-cracks are visible in Figure 7f. Necking is also observed

conditions) on Wiley Online Library for rules of use; OA articles are governed by the applicable Creative Commons



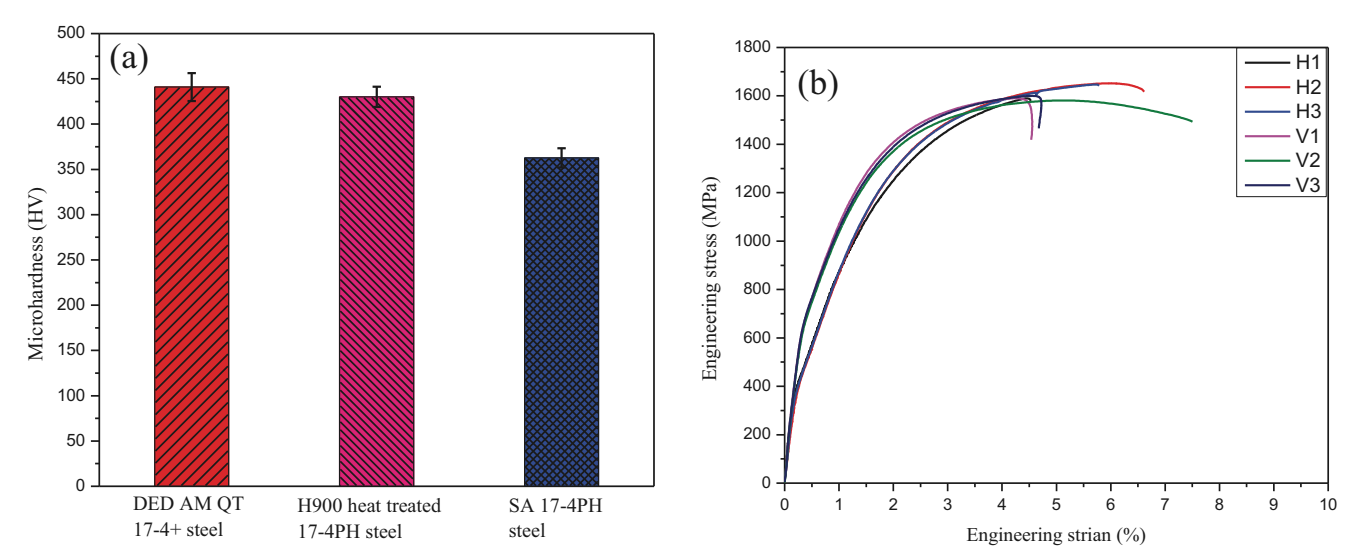


Figure 6. a) Vickers microhardness of as-printed DED QT17-4+ steel, H900-aged wrought 17-4PH steel, and solution-annealed (SA) wrought 17-4PH steel. b) Tensile engineering stress-strain curves of DED'ed QT17-4+ specimens in the as-printed condition, for specimens extracted from horizontally (H1, H2, and H3) and vertically (V1, V2, and V3) built samples, Figure S3 (Supporting Information). Displacement was measured utilizing the digital image correlation (DIC) method and converted into engineering strain.

before fracture occurs, indicating a mixed failure mode, which is compatible with the limited ductility observed in the stress-strain curves (Figure 6).

3. Conclusion

This study utilizes a newly designed QT17-4+ stainless steel powder, originally developed for selective laser melting (SLM) additive manufacturing, for directed energy deposition (DED), for the first time. Process parameters are optimized using density as a response parameter. The response surface methodology (RSM) is used to obtain a predictive density equation. Process parameters, such as laser power, laser scan speed, powder feed rate (PFR), and hatch overlap, are considered. The following conclusions are drawn:

- 1) DED can be used successfully for printing QT 17-4+ stainless steel. The density is optimized using the RSM for different process parameters.
- 2) All first-order factors, except hatch overlap, significantly influence the density. Laser power emerges as the most influential process parameter, positively impacting the density, while laser scan speed negatively affects it.
- 3) The interaction between hatch overlap and laser scan speed significantly reduces the density. The first-order term of scan speed has a smaller impact on density, while hatch overlap does not influence it. The quadratic term of hatch overlap positively influences the density. The interactive terms of PFR and hatch overlap, laser power with hatch overlap, and laser power with PFR have minimal effects on the predicted density. Similarly, the quadratic terms of laser power and laser scan speed minimally affect the density.
- 4) In the as-deposited QT 17-4+ microstructure columnar prior austenite grains are aligned perpendicular to the melt pool

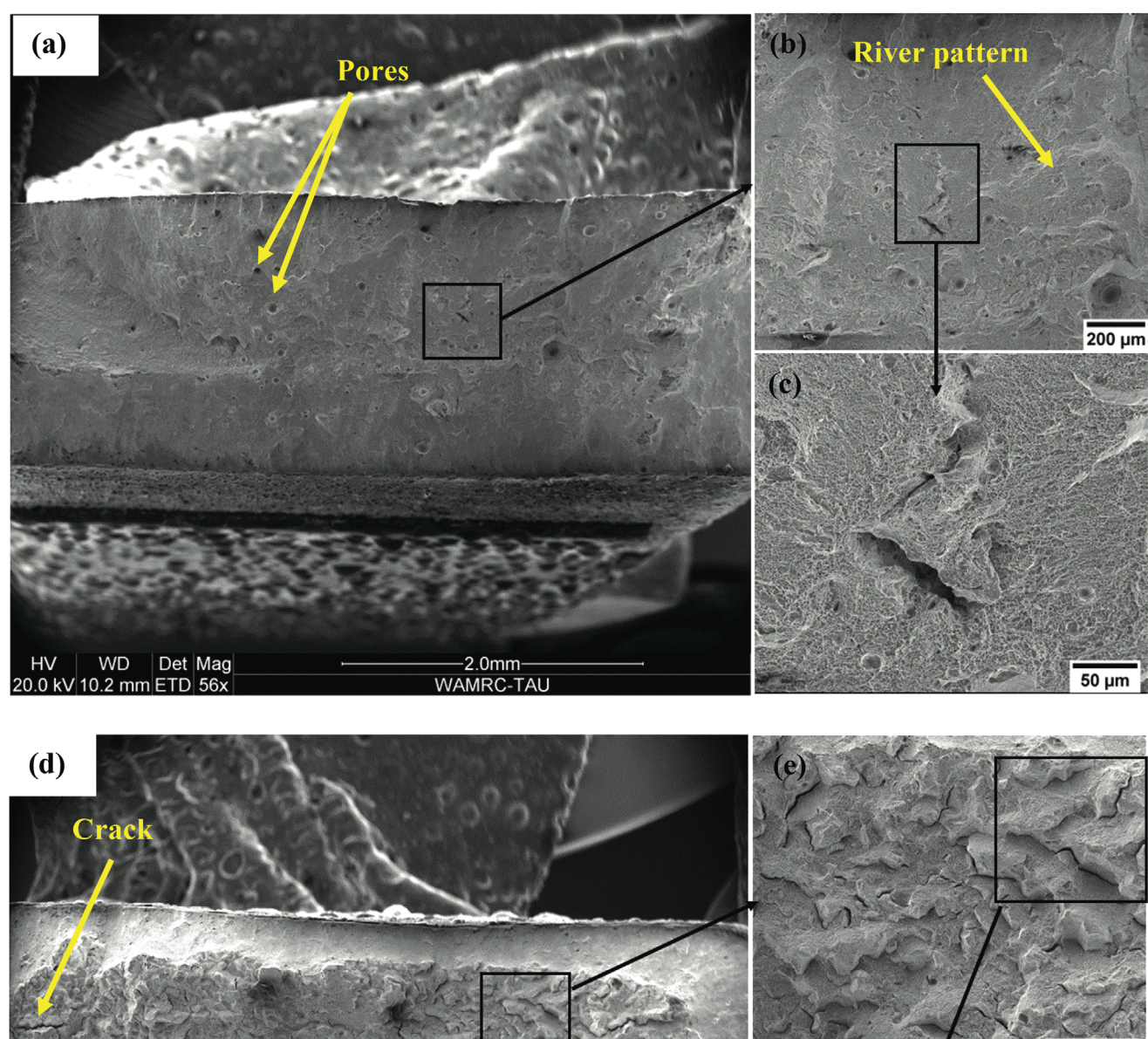
- boundary and along the thermal gradient. Equiaxed grains are observed in the heat-affected zone (interlayer boundary). The microstructure of the DED'ed steel consists of 95% martensite and 5% retained austenite.
- 5) The microhardness of the DED QT 17-4+ steel is higher than that of either solution-annealed or H900-aged 17-4PH wrought steel. The high microhardness of the DED QT 17-4+ steel implies that no post-heat treatments are necessarily required to enhance the strength and hardness of this steel. The yield strength of vertically built samples is higher than that of horizontally built samples. However, the latter have superior ultimate tensile strength. Horizontally built samples exhibit a mixed-mode fracture with predominantly brittle characteristics, whereas vertically deposited samples are characterized by intergranular fracture.

4. Experimental Section

Figure 8 shows the morphology of the received spherical argon atomized QT17-4+ powder. This custom powder was synthesized per demand, especially for DED (recommended particle size range 44–150 $\mu m).$ The powder was designed specifically for additive manufacturing at QuesTek Innovations LLC (Evanston, IL), and argon gas atomized at Praxair, Inc. (Danbury, CT). Chemical composition, particle size distribution (PSD), and particle sphericity tests were performed to verify the quality of the as-synthesized QT17-4+ powder. Figure 8a is a SEM image of several powder particles. Figure 8b,c shows the PSD and sphericity graph of the powder. Camsizer X2 was used to measure the PSD and sphericity of the powder. Camsizer X2 is based on the Dynamic Image Analysis principle (ISO 13322-2) and provides precise powder morphology and size information in the measuring range of 0.8 µm to 8 mm. The D10, D50, and D90 values for the QT17-4+ powder were 60, 77, and 104 µm, respectively. Figure 8c reveals that the average particle sphericity was 0.84 µm. The greater the particle size's sphericity, the better the powder flowability during AM. [68] Table S2 (Supporting Information) presents the chemical composition of the as-synthesized powder and the DED'ed samples.

2365709x, 2024, 15, Downloaded from https://onlinelibrary.wiley.com/doi/10.1002/admt.202400024 by Northw

estern University, Wiley Online Library on [28/08/2024]. See the Terms



Crack

200 µm

(f)

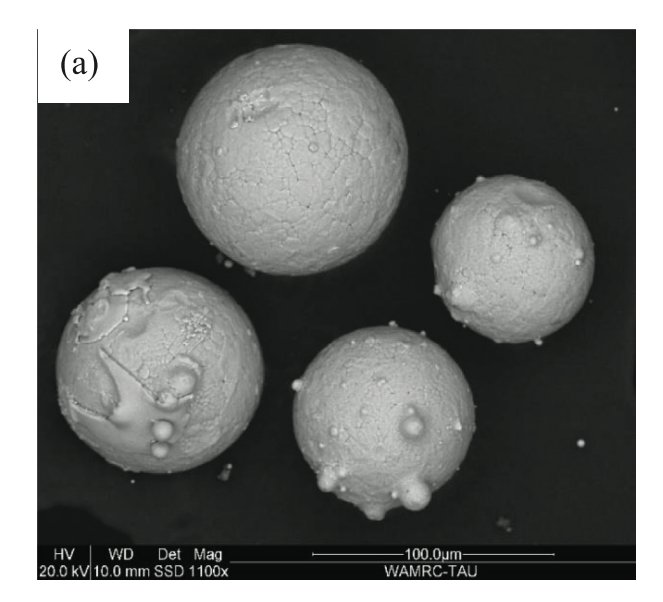
Crack

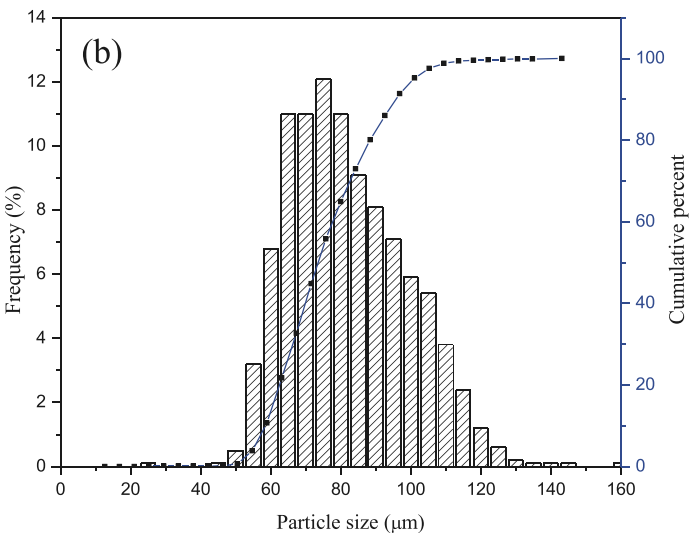
WD Det Mag
200 nm
200 kV 10.4 mm ETD 56x

WAMRC-TAU

Figure 7. Fractographic images of the fractured cross-section of (a–c) horizontally printed sample (H3), (d–f) vertically printed sample (V3) after tensile fracture.

onditions) on Wiley Online Library for rules of use; OA articles are governed by the applicable Creative Commons





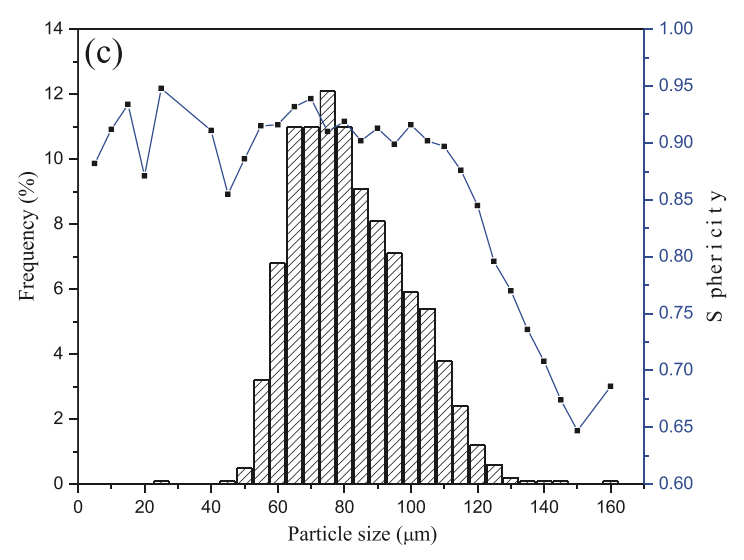


Figure 8. a) SEM image of as-received QT17-4+ powder. b) Particle size distribution of the QT17-4+ powder. c) Sphericity distribution of the powder measured by dynamic image analysis.

The specimens for this study were fabricated using a hybrid Laser Engineered Net Shaping (LENS) DED system from Optomec, Inc. (Albuquerque, NM) operated at Tel-Aviv University's Additive Manufacturing R&D Center. This system is equipped with a 2 kW Nd:YAG laser from IPG Photonics, Inc. (Oxford, MA, USA). The substrate for the experiments was made of stainless steel, with dimensions of $110 \times 110 \times 10$ mm³. Cubic coupons ($10 \times 10 \times 10 \text{ mm}^3$) were fabricated according to an experimental matrix (Table 2) for optimization of process parameters and determination of the effect of the main parameters on the material's density. The density of DED'ed samples was measured utilizing Archimedes' principle according to ASTM B962-13, using a Sartorius BA 210 S analytical balance with $0.\overline{1}\,\text{mg}$ readability and a density analysis kit (Precisa Gravimetrica AG, Dietikon, Switzerland). [69] This approach is considered the most common method to determine the density of AM'ed parts. [70] The weight of polished DED samples was measured both in air and in distilled water. The sample's density was used as the response for the process parameter optimization. The same method was also used to measure the density of the solution-annealed wrought 17-4PH steel.

The DED samples were cut parallel to the build direction for microhardness measurements and microstructural analyses. The cut samples were cold-mounted using EpoFix resin and hardener. The mounted samples were mechanically ground on 320, 800, and 1200-grit SiC papers. The samples were then polished using 9, 3, and 1 µm water-based diamond suspensions. A silica suspension size of 0.05 μm was used for the final polishing step. The polished samples were etched for microstructural characterization (including PAG boundaries) using Kallings' Reagent No. 2 (5 g CuCl₂ + 100 mL HCl + 100 mL ethanol). Microhardness values were measured in the plane perpendicular to the build direction. Microhardness measurements were performed at a load of 200 gf and a 15 s dwell time. Fifteen readings were taken randomly to obtain average microhardness and standard deviation values. Microhardness values were then compared with the values for solution-annealed and H900 (solution heat treatment followed by aging at 480 $^{\circ}\text{C}$ for 1 h) heat-treated wrought 17-4PH steel.

An optical microscope (AX10, ZEISS, Oberkochen, Germany) and SEM (Quanta 200 FEG, FEI, Waltham, MA, USA) were used for microstructural

ADVANCED MATERIALS TECHNOLOGIES

www.advmattechnol.de

characterization. The polished DED'ed samples were imaged under the optical microscope to visualize pores. SEM images were obtained at an accelerating voltage of 20 kV and a 9–10 mm working distance. EBSD was performed with an HKL-Oxford Channel 5 system with a Nordlys II detector, at an inclination of 70° relative to the main beam and a working distance of 15 mm. XRD was conducted for phase analysis of the asreceived QT 17-4+ powder, and DED'ed samples, using a Bruker D8 Discover diffractometer with Cu-K α radiation source ($\lambda=1.5418$ Å) and a Bragg-Brentano set-up. Data point acquisition time per step and step size were set at 0.25 s and 0.02°, respectively. The scan was performed in the two-theta angle range of $40^{\circ}-90^{\circ}$. TOPAS software version 5 was employed for lattice parameter fitting and determination of phase composition.

Section S4.1 and Figure S3 (Supporting Information) show how the tensile samples were cut and prepared. The gauge lengths of the tensile specimens were coated with contrasting speckles. Tensile tests were performed at room temperature using an INSTRON 5582 machine (Norwood, IL, USA). For DIC, the Imager M-lite 9M camera with regular magnification was attached to the LaVision system. The test was performed at a strain rate of $10^{-3}~\text{s}^{-1}$, and images were captured at a rate of one frame per second with a calibrated resolution of 29.516 μm pixel $^{-1}$. DaVis 8.2.0 software was used for DIC post-processing. The ultimate tensile strength (UTS), 0.2% offset yield strength, Young's modulus, and elongation were deduced from the stress-strain plots. Fractographic analysis was carried out on all fracture surfaces, using SEM.

Statistical Analysis: The design of the experiment (DOE) approach was performed using JMP 17.0 data analysis software (SAS Institute Inc., NC, USA). A rotatable central composite design (CCD) was used to create an experimental matrix with 30 patterns. The number of patterns was obtained from Equation (2):

$$N = 2^d + 2d + r \tag{2}$$

where N is the number of experiments, d is the number of factors, and r is the replication of the center point.

CCD had three different types of design points: a) center point; b) factorial point; and c) axial point. Thirty patterns included 16 factorial points, eight axial points, and six replicated center points. Table 1 displays the value of each factor at different factor levels. Table 2 exhibits the experimental matrix with the patterns, factors, and density response data. In Table 2, the center and axial points help estimate the experimental error and curvature of the model. [71,72] To evaluate the effect of laser power (P), scan speed (V), powder feed rate (m), and hatch overlap (H) on the density of the DED'ed QT 17-4+ steel, a five-level CCD was used. In Table 2, patterns with + or – symbols are identified as factorial points, axial points are patterns with either A or a and center points contain only zero. The length of axial points is calculated using the formula 2^{k/4}, where k is the number of factors. The least-squares method was used to obtain the second-order polynomial equation to access the relationship between the response and the factors, Equation (3):[73]

$$\gamma = b_0 + \sum_{j=1}^{k} b_j x_j + \sum_{j=1}^{k-1} \sum_{u=j+1}^{k} b_{ju} x_j x_u + \sum_{j=1}^{k} b_{jj} x_j^2 + \varepsilon$$
 (3)

Herein, y represents the density response, b_0 is the constant term; $b_{j\mu}$, and b_{jj} are the linear interactions and quadratic factors coefficients, respectively. The variable x_i is defined as:

$$x_{j} = \frac{Z_{j} - Z_{j}^{0}}{\Delta Z_{j}}; j = 1, 2, ..., k; Z_{j}^{0} = \frac{Z_{jmax} + Z_{jmin}}{2}; \Delta Z_{j} = \frac{Z_{jmax} - Z_{jmin}}{2}$$
(4)

Here, $Z_{\rm jmax}$ and $Z_{\rm jmin}$ represent the maximum and minimum levels of factor j. The residual error ε is the difference between the observed and predicted values. This empirical formula depicts the relationship between the process parameters and the predicted density obtained using RSM. In all statistical analyses, the t-test significance level was set at p < 0.05, and the F-test lack-of-fit level was set at p > 0.05.

Supporting Information

Supporting Information is available from the Wiley Online Library or from the author.

Acknowledgements

The authors thank the NSF-BSF for funding through grant no. 0605814672 (DMR 2105362), with Dr. Jonathan D. Madison serving as the grant officer. The authors would like to acknowledge the support and valuable information provided by QuesTek Innovations LLC (Evanston IL, Dr. Jason Sebastian, President) concerning the QT17-4+ steel at the inception of this NSF-BSF project.

Conflict of Interest

The authors declare no conflict of interest.

Data Availability Statement

The data that support the findings of this study are available from the corresponding author upon reasonable request.

Keywords

17-4 stainless steel, additive manufacturing (AM), directed energy deposition (DED), QT 17-4+ steel, response surface methodology (RSM)

> Received: January 7, 2024 Revised: April 24, 2024 Published online: May 5, 2024

- [1] W. E. Frazier, J. Mater. Eng. Perform. 2014, 23, 1917.
- [2] D. Herzog, V. Seyda, E. Wycisk, C. Emmelmann, Acta Mater. 2016, 117 371
- [3] Y. C. Shin, N. Bailey, C. Katinas, W. Tan, Comput. Mech. 2018, 61, 617.
- [4] S. Liu, Y. C. Shin, Mater. Des. 2018, 159, 212.
- [5] G. P. Halada, C. R. Clayton, Handbook of Environmental Degradation of Materials, 3rd Ed., William Andrew Publishing, Norwich, NY, 2018, pp. 397–422.
- [6] M. Molitch-Hou, Additive manufacturing, Elsevier, USA 2018, pp. 1– 38.
- [7] R. M. Mahamood, Laser Metal Deposition of Metals and Alloys, Springer, Cham, 2018.
- [8] D. Svetlizky, M. Das, B. Zheng, A. L. Vyatskikh, S. Bose, A. Bandyopadhyay, J. M. Schoenung, E. J. Lavernia, N. Eliaz, *Mater. Today* 2021, 49, 271.
- [9] T. Wang, Y. Y. Zhu, S. Q. Zhang, H. B. Tang, H. M. Wang, J. Alloys Compd. 2015, 632, 505.
- [10] J. Ma, M. M. Atabaki, W. Liu, R. Pillai, B. Kumar, U. Vasudevan, R. Kovacevic, Opt. Laser Technol. 2016, 82, 38.
- [11] J. marc Linares, J. Chaves-Jacob, Q. Lopez, J. M. Sprauel, Rapid Prototyp. J. 2022, 28, 1182.
- [12] R. Bhambroo, S. Roychowdhury, V. Kain, V. S. Raja, *Mater. Sci. Eng. A* 2013, 568, 127.
- [13] H. K. Rafi, D. Pal, N. Patil, T. L. Starr, B. E. Stucker, J. Mater. Eng. Perform. 2014, 23, 4421.
- [14] L. E. Murr, E. Martinez, J. Hernandez, S. Collins, K. N. Amato, S. M. Gaytan, P. W. Shindo, J. Mater. Res. Technol. 2012, 1, 167.

www.advancedsciencenews.com www.advmattechnol.de

- [15] H. K. D. H. Bhadeshia, *Physical Metallurgy*, 5th Ed., Elsevier, Amsterdam, Netherlands, 2014, 1, 2157.
- [16] M. Rouby, P. Blanchard, Stainless Steels, 1993, 139.
- [17] J. A. Shields, Nuclear Technol. 1982, 59, 186.
- [18] T. LeBrun, T. Nakamoto, K. Horikawa, H. Kobayashi, Mater. Des. 2015, 81, 44.
- [19] C. Yu, H. Wang, Z. Yu, Y. Huang, M. Xi, J. Chen, J. Xu, H. Lu, Scr. Mater. 2023, 236, 115673.
- [20] S. Cheruvathur, E. A. Lass, C. E. Campbell, JOM 2016, 68, 930.
- [21] N. Eliaz, N. Foucks, D. Geva, S. Oren, N. Shriki, D. Vaknin, D. Fishman, O. Levi, Materials 2020, 13, 4171.
- [22] B. AlMangour, J. M. Yang, Int. J. Adv. Manuf. Technol. 2017, 90, 119.
- [23] A. Yadollahi, N. Shamsaei, S. M. Thompson, A. Elwany, L. Bian, Int. J. Fatigue 2017, 94, 218.
- [24] B. AlMangour, J. M. Yang, Mater. Des. 2016, 110, 914.
- [25] M. Mahmoudi, A. Elwany, A. Yadollahi, S. M. Thompson, L. Bian, N. Shamsaei, Rapid Prototyp. J. 2017, 23, 280.
- [26] M. J. Bermingham, D. H. StJohn, J. Krynen, S. Tedman-Jones, M. S. Dargusch, Acta Mater. 2019, 168, 261.
- [27] L. E. Murr, E. Martinez, K. N. Amato, S. M. Gaytan, J. Hernandez, D. A. Ramirez, P. W. Shindo, F. Medina, R. B. Wicker, J. Mater. Res. Technol. 2012, 1, 42.
- [28] P. D. Nezhadfar, P. R. Gradl, S. Shao, N. Shamsaei, Jom 2022, 74, 1136.
- [29] L. Pan, C. T. Kwok, B. Niu, X. Huang, Y. Cao, X. Zou, J. Yi, J. Mater. Res. Technol. 2023, 23, 1296.
- [30] Y. Li, H. Yang, X. Lin, W. Huang, J. Li, Y. Zhou, Mater. Sci. Eng. A 2003, 360, 18.
- [31] K. Zhang, S. Wang, W. Liu, X. Shang, Mater. Des. 2014, 55, 104.
- [32] E. Amar, V. Popov, V. M. Sharma, S. Andreev Batat, D. Halperin, N. Eliaz. Materials 2023, 16, 7253.
- [33] C. Morales, M. Merlin, A. Fortini, A. Fortunato, Coatings 2023, 13, 11.
- [34] A. K. Sood, R. K. Ohdar, S. S. Mahapatra, J. Adv. Res. 2012, 3, 81.
- [35] T. Najib, M. Solgi, A. Farazmand, S. M. Heydarian, B. Nasernejad, J. Environ. Chem. Eng. 2017, 5, 3256.
- [36] G. Banerjee, S. Car, J. S. Scott-Craig, M. S. Borrusch, N. Aslam, J. D. Walton, Biotechnol. Bioeng. 2010, 106, 707.
- [37] H. S. Arruda, G. A. Pereira, G. M. Pastore, Food Anal. Meth. 2017, 10, 100
- [38] R. Li, J. Liu, Y. Shi, M. Du, Z. Xie, J. Mater. Eng. Perform. 2010, 19, 666.
- [39] A. N. Jinoop, C. P. Paul, S. K. Mishra, K. S. Bindra, Vacuum 2019, 166, 270.
- [40] H. L. Wei, Y. Cao, W. H. Liao, T. T. Liu, Addit. Manuf. 2020, 34, 101221.
- [41] H. Fayazfar, M. Salarian, A. Rogalsky, D. Sarker, P. Russo, V. Paserin, E. Toyserkani, *Mater. Des.* 2018, 144, 98.
- [42] J. Choi, Y. Chang, Int. J. Mach. Tools Manuf. 2005, 45, 597.
- [43] S. Wolff, T. Lee, E. Faierson, K. Ehmann, J. Cao, J. Manuf. Process. 2016, 24, 397.
- [44] R. F. Hamilton, B. A. Bimber, T. A. Palmer, J. Alloys Compd. 2018, 739, 712

- [45] T. DebRoy, H. L. Wei, J. S. Zuback, T. Mukherjee, J. W. Elmer, J. O. Milewski, A. M. Beese, A. Wilson-Heid, A. De, W. Zhang, Prog. Mater. Sci. 2018, 92, 112.
- [46] X. P. Li, C. W. Kang, H. Huang, T. B. Sercombe, Mater. Des. 2014, 63, 407
- [47] I. Mathoho, E. T. Akinlabi, N. Arthur, M. Tlotleng, CIRP J. Manuf. Sci. Technol. 2020, 31, 450.
- [48] J. S. Kim, B. J. Kang, S. W. Lee, J. Mech. Sci. Technol. 2019, 33, 5731.
- [49] J. L. Bennett, S. J. Wolff, G. Hyatt, K. Ehmann, J. Cao, J. Manuf. Process. 2017, 28, 550.
- [50] J. Bennett, S. Wolff, G. Hyatt, J. Cao, J. Manuf. Process 2017, 28, 550.
- [51] U. de Oliveira, V. Ocelík, J. T. M. De Hosson, Surf. Coatings Technol. 2005, 197, 127.
- [52] D. G. Ahn, Int. J. Precis. Eng. Manuf. Green Technol. 2021, 8, 703.
- [53] K. Kempen, B. Vrancken, S. Buls, L. Thijs, J. Van Humbeeck, J. P. Kruth, J. Manuf. Sci. Eng. Trans. ASME 2014, 136, 061026.
- [54] T. Nakamoto, N. Shirakawa, Y. Miyata, H. Inui, J. Mater. Process. Technol. 2009, 209, 5653.
- [55] R. Mertens, B. Vrancken, N. Holmstock, Y. Kinds, J. P. Kruth, J. Van Humbeeck, Phys. Procedia. 2016, 83, 882.
- [56] M. Hemachandra, S. Thapliyal, K. Adepu, J. Mater. Sci. 2022, 57, 17139.
- [57] Y. Yang, Y. Zhu, H. Yang, J. Tribol. 2020, 142, 111701.
- [58] Y. J. Liang, X. Cheng, H. M. Wang, Acta Mater. 2016, 118, 17.
- [59] A. V. Kartavykh, V. V. Tcherdyntsev, M. V. Gorshenkov, S. D. Kaloshkin, J. Alloys Compd. 2014, 586, S180.
- [60] J. D. Hunt, Mater. Sci. Eng. 1984, 65, 75.
- [61] J. Lapin, Z. Gabalcová, Intermetallics 2011, 19, 797.
- [62] P. Liu, Z. Wang, Y. Xiao, M. F. Horstemeyer, X. Cui, L. Chen, Addit. Manuf. 2019, 26, 22.
- [63] H. Gungunes, E. Yasar, T. N. Durlu, J. Mater. Sci. 2007, 42, 6102.
- [64] T. Karthikeyan, M. K. Dash, S. Saroja, M. Vijayalakshmi, Micron 2015, 68, 77.
- [65] F. J. Humphreys, I. Brough, Microsc. Microanal. 1999, 5, 240.
- [66] W. Choo, M. Ebrahimian, K. Choi, J. H. Kim, Met. Mater. Int. 2023, 29, 1750.
- [67] H. Eskandari, H. R. Lashgari, L. Ye, M. Eizadjou, H. Wang, Mater. Today Commun. 2022, 30, 103075.
- [68] Y. Zhao, Y. Cui, Y. Hasebe, H. Bian, K. Yamanaka, K. Aoyagi, T. Hagisawa, A. Chiba, Powder Technol. 2021, 393, 482.
- [69] ASTM International, Astm B962-13 2013.
- [70] A. B. Spierings, M. Schneider, R. Eggenberger, Rapid Prototyp. J. 2011, 17, 380.
- [71] G. Sado, M. C. Sado, Les plans d'expériences: de l'expérimentation à l'assurance qualité, AFNOR, Paris **1991**, pp. 1–261.
- [72] A. I. Usman, A. A. Aziz, B. K. Sodipo, SN Appl. Sci. 2019, 1, 403.
- [73] W. Djoudi, F. Aissani-Benissad, S. Bourouina-Bacha, Chem. Eng. J. 2007, 133, 1.
- [74] A. Saboo, R. Komai, D. Frankel, M. Thomas, G. Olson, US20230134452A, U.S. Patent and Trademark Office, 2023.